MATERIALS CHEMISTRY FRONTIERS

RESEARCH ARTICLE

View Article Online
View Journal | View Issue

Cite this: *Mater. Chem. Front.*, 2023, **7**, 5941

Morphological control of $Ca_xMn_{1-x}Nb_2O_6$ columbites for use as lithium hosts in batteries†

Wilgner Lima da Silva, [ae] Marc Walker, [b] Rogério M. Ribas, [c] Robson S. Monteiro, [c] Emma Kendrick *[d] and Richard I. Walton *[a]

Received 27th May 2023,
Accepted 7th October 2023

DOI: 10.1039/d3qm00604b

rsc.li/frontiers-materials

Ternary niobium-based oxides have shown great potential as negative electrodes for Li-ion batteries due to their structural stability and high-rate capabilities. A hydrothermal reaction at 240 °C is used to synthesise $MnNb_2O_6$ (MNO) from different alkaline MOH solutions with M = Li, Na, K, yielding MNO-Li, MNO-Na, and MNO-K and a new phase, $Ca_{0.25}Mn_{0.75}Nb_2O_6$ (CMNO). The MNO materials were characterised structurally using powder X-ray diffraction revealing that they have disordered columbite structures, with Mn and Nb randomly distributed over octahedral sites, which become ordered upon annealing at 1000 °C. In contrast, CMNO has an ordered structure, which may be due to the larger ionic radius of Ca^{2+}. Only 25% of Mn can be replaced by Ca. The crystalline morphology of the samples is dependent on the synthesis medium, with intricately shaped particles of 10s of nm using SEM. Spectroscopic studies (XPS and XAFS) confirm the Mn^{2+} oxidation state in all materials. MNO-Na has higher cyclability towards Li uptake with capacity retention of 64% and specific capacity of 182 mA h g^{-1} after 200 cycles. CMNO showed the highest capacity after 50 cycles, 142 mA h g^{-1}, which indicates that structure expansion controls the quantity of Li inserted. *Ex situ* PXRD studies revealed that all materials undergo a conversion reaction during the first lithiation although MNO-Na and MNO show better structural stability regaining their crystallinity after the first delithiation. Electrochemical impedance spectroscopy reveals a complex Li lithiation/delithiation mechanism at different voltages.

1. Introduction

Li-ion batteries have relied on graphite as the negative electrode (anode), which has a theoretical capacity of 372 mA h g^{-1}.[1–4] Li metal (−3.04 V *vs.* SHE)[5] allows an operating voltage of 4 V due to its negative potential compared to metal oxides or hard carbon-based anodes.[5] Anode materials that operate at higher average potentials improve safety, inhibit dendrite formation and, to some extent, limit solid electrolyte interphase (SEI) formation.[6] $Li_4Ti_5O_{12}$ has a high voltage plateau at ∼1.5 V *vs.* Li/Li^+,[7] and Nb-based oxides ∼1.6 V *vs.* Li/Li^+ 1.0–3.0 V,[8] and exhibit high rate, suitable for power tools and other devices.

To increase the energy density further from graphite based negative electrodes,[9] either higher capacity negative electrodes are required, or high voltage cathode materials can be partnered with higher average operating voltage anodes, where both systems are still within the voltage stability window of the electrolyte.

With the widespread increase of Li-ion batteries for electric vehicles, portable devices, and stationary batteries for industrial power,[1,10] novel materials that achieve high-rate and high energies, synthesised *via* sustainable routes are essential. Metal oxides provide an alternative to replace carbon-based anodes in Li-ion batteries.[6,8] In particular, niobium-based oxides have received recent attention because of their potential in Li-ion storage with higher specific capacities, and capabilities of steady operation at high working voltage without Li dendrite formation and high Li^+ diffusion coefficients owing to their open structures.[3,8,11] $TiNb_2O_7$ is one of the many examples of anode materials for Li-ion batteries, which has attracted attention due to its high theoretical capacity (388 mA h g^{-1}, corresponding to 5 Li^+ per formula unit) and structural stability.[3,11–13] Nonetheless, improvements in electronic and ion conductivities are required for capacity retention and rate capability, thus, motivating the search for other anode materials with more available transition metals than Ti.

[a] *Department of Chemistry, University of Warwick, Gibbet Hill Road, Coventry CV4 7AL, UK. E-mail: r.i.walton@warwick.ac.uk*
[b] *Department of Physics, University of Warwick, Gibbet Hill Road, Coventry CV4 7AL, UK*
[c] *Companhia Brasileira de Metalurgia e Mineração (CBMM), Araxá, Minas Gerais 38183-903, Brazil*
[d] *School of Metallurgy and Materials, University of Birmingham, Edgbaston, Birmingham B15 2TT, UK. E-mail: e.kendrick@bham.ac.uk*
[e] *WMG, University of Warwick, Gibbet Hill Road, Coventry CV4 7AL, UK*

† Electronic supplementary information (ESI) available. See DOI: https://doi.org/10.1039/d3qm00604b

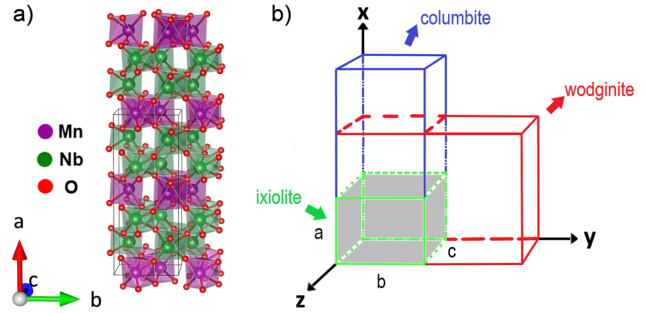

Fig. 1 (a) Polyhedral view of the $MnNb_2O_6$ columbite crystal structure and (b) the relationship between the unit cells of ixiolite, columbite and wodginite.

The AB_2O_6 columbite structure has two different octahedral sites (O_h), one occupied by divalent cations, Mn, Cu, Zn, Co, Ni *etc.*, in the A sites and the other by pentavalent cations, Ta or Nb, in the B sites. As an α-PbO_2 superstructure, $MnNb_2O_6$ crystallises in an orthorhombic space group *Pbcn* having a slightly distorted hexagonal closed-packed oxygen sublattice. This layered structure has MnO_6 and NbO_6 O_h with common edges staggered in zigzag chains along the *c*-axis and alternating O_h along *a* with a –Mn–Nb–Nb–Mn– sequence.[14–17] Because of interstitial sites, shown in Fig. 1, it can accommodate Li-ions upon electrochemical lithiation as shown by reported electrochemical studies.[18] However, the type of Li-mechanism has not been investigated. By chemically targeting the composition and choice of transition metals, the layered structure can be contracted or expanded, which can potentially be a way of tuning the quantity of inserted lithium.

The structure of the mineral columbite $(Fe,Mn)(Nb,Ta)_2O_6$ and annealed samples have been investigated through combining laboratory X-ray and neutron diffraction refinements and ^{57}Fe Mössbauer spectroscopy.[14,19,20] These studies concluded that interlayer mixing between A and B exists. In the extreme case the ixiolite structure is observed.[14] Its unit cell is 1/3 of the columbite unit cell, with simplified formula of MO_2, with M = Mn, Ta, Fe and Nb, *i.e.*, complete disorder of the various constituent cations.[21] Natural samples have been found to also crystallise in a monoclinic unit cell four times the unit cell volume of ixiolite, known as wodginite,[21] Fig. 1.

The hydrothermal synthesis of $MnNb_2O_6$ has been reported before in a two-step method in KOH solution.[15,22–26] The first step consisted of a reaction of a Nb precursor (generally Nb_2O_5) with KOH to produce an hexaniobate anion $[Nb_6O_{19}]^{8-}$ solution, which in a second step was reacted with a transition metal (M^{2+}) solution. There is no reported substantial characterisation of the bulk structure of these materials when made hydrothermally and only a few investigations have annealed the as-made samples, which decreases surface area by increased particle size, eliminating any morphology associated with the synthetic method and may remove any structural disorder. Herein, we present a study of the hydrothermal synthesis of $MnNb_2O_6$ in different aqueous hydroxide media, LiOH, NaOH and KOH and an investigation of Ca substitution to form $Ca_xMn_{1-x}Nb_2O_6$. We have explored the thermal stability of these samples, which proved that the samples are pure even after sintering in air at 1000 °C, when they became more crystalline. Importantly, the samples show different electrochemical properties based on the base used in synthesis, which may be due to crystal morphology. Only 25% of Ca^{2+} can be introduced into the structure, which has the effect of giving an ordered structure, compared to the parent niobate and further affects the behaviour towards Li uptake. Conversion reaction occurs upon lithiation for the reported samples, as described for Mn[27,28] and Mo[29–31]-based oxides.

2. Experimental

2.1. Materials synthesis

Ammonium niobium oxalate hydrate (ANO, $NH_4(NbO(C_2O_4))_2$-$(H_2O)_2{\cdot}xH_2O$, CBMM, 1.57 mmol), and $MnSO_4{\cdot}H_2O$ (Sigma-Aldrich, 99%, 0.785 mmol), were dissolved in 7 mL of deionised H_2O (2 : 1 molar ratio). To this solution 9.4 mmol of $LiOH{\cdot}H_2O$ (Alfa Aesar, 98.5%), NaOH (Fisher Scientific, 99.4%) or KOH (Fisher Scientific, 85%) was added, and the resulting mixture was stirred at room temperature for 15 min. The reaction vessel was sealed inside a 20 mL Teflon-lined stainless-steel autoclave and heated for 18 hours at 240 °C. To obtain large amounts of $MnNb_2O_6$, the reaction was scaled-up using 200 mL Teflon-lined stainless-steel autoclaves, using respectively, 0.0224, 0.0448, and 0.27 mol of niobium, manganese precursors and alkaline base. These were dissolved in 100 mL of deionised water, stirred for 30 min, and heated for 18 hours at 240 °C.

$Ca_{0.25}Mn_{0.75}Nb_2O_6$ was hydrothermally synthesised by substituting 25% of $MnSO_4{\cdot}H_2O$ with CaO (Riedel-de Haen, 99%). CaO was previously dried at 70 °C. Small batches were synthesised by stirring the precursors in 7 mL of deionised water in a 20 mL Teflon-lined stainless-steel autoclaves for 15 min. Large batches of Ca-substituted columbite were obtained in 100 mL of deionised water in a 200 mL stainless-steel autoclave by increasing the amounts from small batches by a factor of 14.29. For this, the precursors were stirred for 2 hours prior to heating the vessel for 18 hours at 240 °C. Higher levels of Ca-substitution were attempted, but this led to materials contaminated with $CaNb_2O_6$ columbite or an extra phase not indexed (see ESI†).

The yellow solid product was washed with deionised water and collected *via* vacuum filtration, before drying at 70 °C in air for 24 hours. To remove small amounts of $MnCO_3$ impurity (see ESI†), 0.5 M acetic acid (53 mL of solution for every gram of sample) solution was used, and the synthesised powder stirred at room temperature for 24 hours. The solid was filtered, washed with deionised water at 80 °C (150 mL) and propan-2-ol (50 mL). The material was dried in a drying oven at 70 °C for 24 hours. The procedure was repeated until the samples were pure, as confirmed by powder X-ray diffraction.

Samples were sintered in air at 1000 °C for 4 hours in a muffle furnace with cooling and heating rates of 10 °C min^{-1}.

2.2. Analytical techniques

The structural characteristics of the as-prepared samples were determined by powder X-ray diffraction (PXRD) using a Panalytical Empyrean instrument with Cu $K_{\alpha 1/2}$ radiation and were recorded between 10°–80° 2θ. For crystal structure refinement, PXRD was collected with Cu $K_{\alpha 1}$ radiation between 10°–100° 2θ using a Panalytical X-Pert Pro MPD diffractometer. The software GSAS II[32] was used to fit the diffraction profile and refine crystal structures. *Ex situ* PXRD analysis of electrodes after use was carried out in an argon atmosphere in a domed sample holder (Anton Paar) after decrimping half-coin cells inside an argon-filled glovebox. PXRD as a function of temperature were recorded using a Bruker D8 instrument with Cu $K_{\alpha 1/2}$ radiation. Samples were heated from room temperature to 800 °C in air and XRD patterns were recorded at intervals of 50 °C (100°–700 °C) and 25 °C (700°–800 °C) between 15°–90° 2θ.

The morphology of the samples was observed by scanning electron microscopy (SEM) coupled with energy-dispersive X-ray spectroscopy (EDS) (Zeiss Sigma FEG-SEM). Samples were ultrasonically dispersed in a few millilitres of propan-2-ol. This suspension was drop casted onto a Si wafer and then allowed to dry at 70 °C for a few minutes before imaging. SEM from ball-milled samples with carbon black (C65) were dusted onto stubs coated with adhesive carbon tabs for imaging. EDS maps were measured from samples heavily covered onto carbon tabs to improve X-ray emission. SEM-EDS of electrodes after the first cycle was performed. Electrodes were loaded onto carbon tabs in an airtight transfer box in an argon filled glovebox.

Brunauer–Emmett–Teller (BET) analysis of N_2 absorption/desorption isotherms was used to measure surface area and pore size using a Micromeritics ASAP 2020 surface area and porosity apparatus. The samples were dried by heating to 150 °C under vacuum on the preparation system for 8 hours then transferred to the instrument.

FTIR spectra were recorded using an Agilent Cary 620 spectrometer over a wavenumber range of 650 to 4000 cm^{-1} to examine the presence of H_2O and carbonate in the samples (see ESI†). X-ray fluorescence (XRF) spectroscopy was carried out to determine the elemental composition of samples using a Rigaku ZXS Primus IV instrument.

The surface composition and transition metal valence state from the particle surface of as-synthesised and annealed materials were determined by X-ray photoelectron spectroscopy (XPS). XPS data were collected on a Kratos AXIS Ultra DLD ultrahigh vacuum system with a base pressure of 5×10^{-11} mbar. Ball milled samples were characterised in an Omicron Multiprobe instrument with typical operating pressure 2×10^{-11} mbar. XPS data in both instruments were collected using Al K_α X-rays ($h\nu$ = 1486.7 eV) at a take-off angle of 90° with respect to the surface plane of the sample. All data were analysed using the CasaXPS package,[33] utilising mixed Gaussian–Lorentzian line shapes and Shirley backgrounds.

Mn K-edge X-ray absorption spectroscopy was measured on Beamline B18[34] of the Diamond Light Source, UK, for $MnNb_2O_6$ samples. Samples were diluted with polyethylene powder and pressed into 13 mm pellets of approximately 1 mm thick to optimise the absorption measurements, which were collected in transmission mode and normalised using the ATHENA software package.[35] For analysis of X-ray absorption near-edge structure (XANES), $MnSO_4{\cdot}H_2O$, Mn_2O_3 and MnO_2 were used as standards and the edge energy (eV) was compared using the energy of normalised absorption at 0.5. Extended X-ray absorption fine structure (EXAFS) were analysed using the ARTEMIS software package.[35]

Thermogravimetric analysis (TGA) and differential thermal analysis (DTA) were performed on an instrument Mettler Toledo TGA/DSC Star^e system, with a heating rate of 10 °C min^{-1} under air to determine the water content of as-made samples.

2.3. Electrode preparation

Electrochemical performance was evaluated using CR2032 coin-type lithium metal (half) cells assembled in an argon-filled glovebox.

As-synthesised powders were sieved to 50 μm (Sieve shaker EFL 300). The as-made samples were dried under vacuum at 200 °C for 24 hours prior ball milling. The powder was added to a 50 mL ball mill pots with zirconia spheres as grinding media in a 1 : 1.5 mass ratio (powder to grinding medium) with C65 carbon black and milled for 2 h at 200 rpm with 1 min breaks every 10 min. A few drops of propan-2-ol were added to avoid sticking.

Negative electrodes were prepared by drying the milled samples for 24 hours at 200 °C under vacuum, which were then co-dispersed with the remaining 5 wt% C65 and polyvinylidene fluoride (PVDF 5130, Solvay) (8 wt% solution in 1-methylpyrrolidin-2-one (NMP), anhydrous 99.5%, Sigma Aldrich), in an 80 : 10 : 10 ratio in wt%. The ball-milled active material was mixed with NMP using a THINKYMIXER ARE-250 at 1000 rpm (2 × 5 min). C65 was added and mixed (2 × 5 min) at 2000 rpm, following addition of PVDF with further mixing (3 × 5 min). The ink was coated onto Cu foil using a doctor blade at 200 μm. The electrode was subsequently dried at 80 °C with further vacuum drying at 60 °C for 24 hours. Anode discs (15 mm) were cut out, dried at 120 °C for 24 hours under vacuum, and half coin cells were assembled against metallic lithium, incorporating Celgard 2325 as the separator. 60 μL of an electrolyte of 1.0 M $LiPF_6$ dissolved in ethylene carbonate : ethyl methyl carbonate in a 1 : 1 ratio with 1% vinylene carbonate, were used (Soulbrain, PuriEL). Galvanostatic charge/discharge was performed on a BioLogic BCS potentiostat at room temperature (25 °C) under constant currents limiting the voltage window. Electrochemical impedance spectroscopy (EIS) was measured during lithiation/delithiation at 1.0, 0.75, 0.25 V *vs.* Li/Li^+ at the 22nd cycle (6 voltage points) (1st cycle – formation at 10 mA g^{-1}, 20 cycles at 200 mA g^{-1} and last cycle at 10 mA g^{-1}) under a constant voltage step at 1 mA g^{-1} for 30 min, followed by a rest step for 30 min, in the frequency range from 1 MHz to 50 mHz with an amplitude of 2 mV.

3. Results and discussion

The hydrothermal reaction between ANO and $MnSO_4$ gave samples whose PXRD patterns can be indexed to an orthorhombic unit cell. The PXRD patterns from the as-synthesised $MnNb_2O_6$ in different bases Li (MNO-Li), Na (MNO-Na), and K (MNO-K) hydroxides, however, do not show the (200) and (110) peaks associated with an ordered orthorhombic unit cell between 10° and 20° 2θ, Fig. 2. This could be an indication that hydrothermally samples are disordered and have an ixiolite unit cell, with random occupancy of Mn and Nb over the O_h sites. On the other hand, $Ca_{0.25}Mn_{0.75}Nb_2O_6$ (CMNO) can be indexed to an orthorhombic unit cell with evidence for the ordered columbite structure, indicated by the presence of the low-angle (200) and (110) peaks between 10°–20° 2θ, Fig. 2.

To find the best model to refine the crystal structure of the samples and understand the relationship of order and disorder, simulations of the diffraction pattern were made by increasing the interlayer mixing of Nb and Mn sites. Fig. S4 (ESI†) shows the effect of an increase in disorder associated with the swapping of Mn and Nb over available sites. Using the ixiolite model provides the best refinement of the Mn samples and was used to fit the diffraction patterns of MNO-Li, MNO-Na, and MNO-K, with the results shown in Fig. 2(a)–(c). CMNO refinement used an orthorhombic model, Fig. 2d. Table 1 shows the refined structural parameters and fit statistics, where lattice parameters of some literature materials are provided for comparison.

Besides testing the orthorhombic (Fig. S4b, ESI†) and ixiolite models, refinements using a two-phase combination of columbite and ixiolite or of ixiolite and monoclinic ($Mn(Mn_{0.333}Nb_{0.666})Nb_2O_8$) unit cells were tested for MNO-Na PXRD (Fig. S5, ESI†). These always converged towards a single ixiolite phase, Table S1 (ESI†), supporting the conclusion that ixiolite is the best available structural model for the as-made MNO materials.

After annealing, the samples became more crystalline and ordered as seen by the appearance of (200) and (110) Bragg peaks, Fig. 3, characteristic of an ordered orthorhombic unit cell, but no other features emerged. This confirms that all samples were pure as made. The Rietveld refinement of all annealed samples indicates that MNO-Li has Nb_2O_5 (Table S2 and Fig. S6a, ESI†) as a minor impurity, corresponding to a phase fraction of 0.01%. MNO-Na has a very small fraction of an impurity, which could not be indexed, but was added as part of the background to refine the model. MNO-K was found to be phase pure. Table 2 give details on the refined structural parameters, and Table S3 (ESI†) lists the peaks added as background in the MNO-Na refinement shown in Fig. S6b (ESI†).

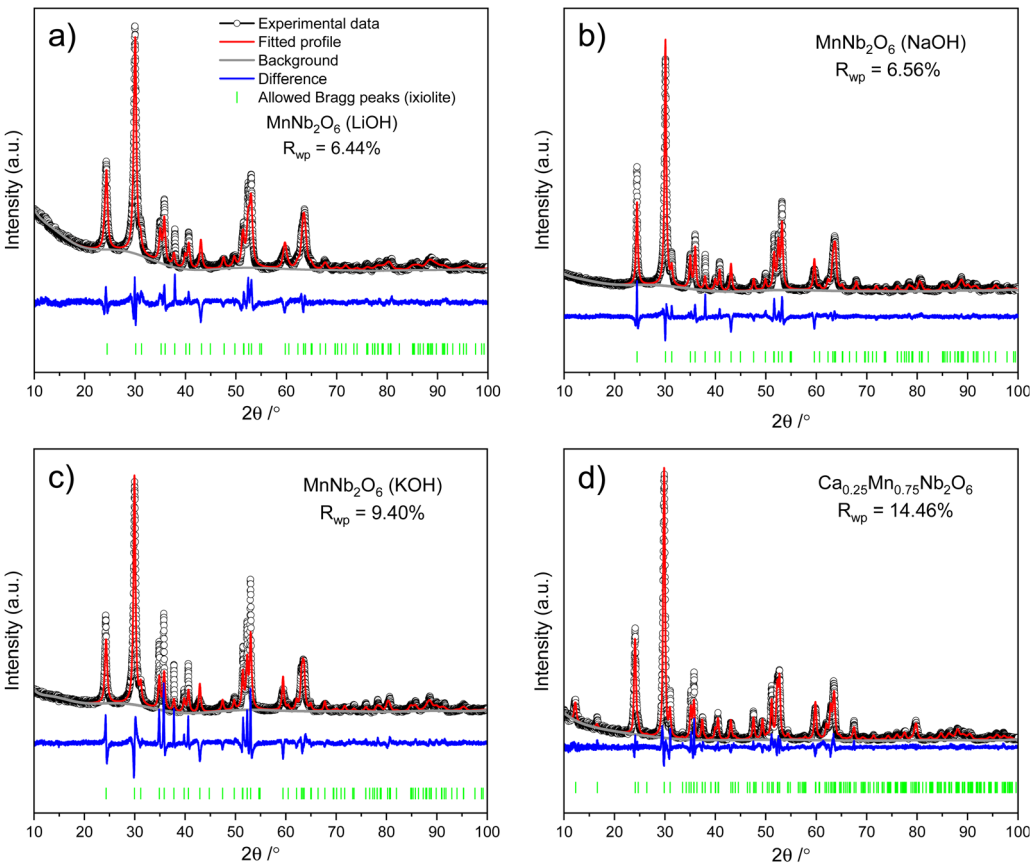

Fig. 2 Rietveld refinement of the as-made samples (a) MNO-Li, (b) MNO-Na, (c) MNO-K using an ixiolite crystal structure, and (d) CMNO using an orthorhombic structure performed against PXRD data (λ = 1.54056 Å).

Table 1 Structural parameters obtained from Rietveld refinement against PXRD data from as-made MNO-Li, MNO-Na, MNO-K and CMNO

Atom	x	y	z	Occupancy	Site	U_{iso}/Å^2
$MnNb_2O_6$ (LiOH) (as made) R_{wp} = 6.46%, GOF = 2.70, a = 4.7751(5) Å, b = 5.7581(5) Å, c = 5.1324(5) Å, vol = 141.12(1) Å^3, ρ = 5.2238 g cm^{-3}						
Mn	0.0	0.3357(3)	0.25	0.37(2)	4c	0.0204(7)
Nb	0.0	0.3357(3)	0.25	0.63(2)	4c	0.0204(7)
O	0.268(9)	0.116(1)	0.079(1)	1.0	8d	0.00197*
* fixed						
$MnNb_2O_6$ (NaOH) (as made) R_{wp} = 6.56%, GOF = 2.52, a = 4.7610(3) Å, b = 5.7385(3) Å, c = 5.1473(3) Å, vol = 140.63(8) Å^3, ρ = 5.1683 g cm^{-3}						
Mn	0.0	0.3327(2)	0.25	0.41(2)	4c	0.0176(5)
Nb	0.0	0.3327(2)	0.25	0.59(2)	4c	0.0176(5)
O	0.2647(7)	0.11(1)	0.0808(8)	1.0	8d	0.018(1)
$MnNb_2O_6$ (KOH) (as made) R_{wp} = 9.40%, GOF = 3.91, a = 4.7668(6) Å, b = 5.7635(7) Å, c = 5.1512(6) Å, vol = 141.03(4) Å^3, ρ = 5.2125 g cm^{-3}						
Mn	0.0	0.3334(3)	0.25	0.38(2)	4c	0.0197(8)
Nb	0.0	0.3334(3)	0.25	0.63(2)	4c	0.0197(8)
O	0.260(1)	0.126(1)	0.087(1)	1.0	8d	0.003(2)
$Ca_{0.25}Mn_{0.75}Nb_2O_6$ (as-made) R_{wp} = 14.62%, GOF = 1.67, a = 14.4365(8) Å, b = 5.7731(3) Å, c = 5.1109(3) Å, vol = 425.96(3) Å^3, ρ = 5.2212 g cm^{-3}						
Mn	0.0	0.3190(8)	0.25	0.87(4)	4c	0.013(2)
Ca	0.0	0.3190(8)	0.25	0.13(4)	4c	0.013(2)
Nb	0.3356(1)	0.3216(2)	0.2397(6)	1.0	8d	0.0139(5)
O	0.1079(3)	0.108(1)	0.056(1)	1.0	8d	0.025(4)
O'	0.4182(6)	0.115(2)	0.088(2)	1.0	8d	0.01957
O''	0.7614(8)	0.123(2)	0.083(3)	1.0	8d	0.034(4)

$(Ta_{1.73}Fe_{0.72}Sn_{0.52}Nb_{0.52}Mn_{0.48})O_8$ ixiolite (previously reported[36]) a = 4.742 Å, b = 5.731 Å, c = 5.152 Å, vol = 140.01 Å^3, ρ = 7.39 g cm^{-3}. Collection code ICSD 45150

$MnNb_2O_6$ orthorhombic (previously reported[37]) a = 14.4376(3) Å, b = 5.7665(1) Å, c = 5.0841(1) Å, Vol = 423.27 Å^3, ρ = 5.28 g cm^{-3}. Collection code ICSD 151724

$CaNb_2O_6$ (previously reported[38]) a = 14.956(4) Å, b = 5.752(4) Å, c = 5.204(4) Å, Vol = 446.79 Å^3, ρ = 4.79 g cm^{-3}. Collection code ICSD 15208

CMNO has a slightly bigger unit cell than $MnNb_2O_6$[37] and smaller than $CaNb_2O_6$,[38] proving the substitution of Mn by Ca. The composition determined from the refinement $Ca_{0.13}Mn_{0.87}Nb_2O_6$ is close to that expected. *In situ* PXRD heating of CMNO indicated no phase transition or further segregation between Ca/Mn sites (Fig. S7, ESI†). After annealing, the calculated composition ($Ca_{0.22}Mn_{0.78}Nb_2O_6$) is closer to the expected stoichiometry. The small difference between the calculated composition between as-synthesised and annealed refinements could be associated to reduction of peak anisotropy, which improved the model fitting. Compared with the XRF result ($Ca_{0.13}Mn_{0.69}Nb_{2.00}O_{5.82}$), the composition obtained from the Rietveld refinements of CMNO for both as-made and sintered samples are comparable.

TGA/DSC revealed total mass losses of 3.7, 3.1, 1.9 and 1.2% for samples MNO-Li, MNO-Na, MNO-K, and CMNO, respectively, Fig. S8 (ESI†). The water content on these samples is low, as expected, and it is probably due to surface adsorption.

XANES spectra, Fig. 4(a) and (b), confirm that all samples have divalent Mn. EXAFS data were analysed to model order/disorder within the stacking layers surrounding Mn atoms. However, comparing fits determined that 50% Mn and Nb site mixing generates a similar result as an ordered model (Fig. S9 and Table S4, ESI†). In the case of the series of naturally occurring $(Fe_xMn_{1-x})(Ta_yNb_{2-y})O_6$, site mixing between Mn and Fe O_h sites in the TaO_6 and NbO_6 was found when neutron and PXRD refinements were combined.[14] Tarantino *et al.*[20] showed for a series of $(Mn,Fe)Nb_2O_6$ that the EXAFS data have small composition dependence in the first shell (metal–oxygen bond lengths from Mn K- and Fe K-edges), which suggests that differences between the local structure of an ordered or disordered MNO would be minor, and it agrees with the observations here made.

The N_2 adsorption of the as-synthesised materials shows a Type III isotherm, which agrees with Wang *et al.*[22] and Lee *et al.*[18] who reported results from hydrothermally made and solvothermal/thermally treated $MnNb_2O_6$ (Fig. S10, ESI†). This is typical of a material with relatively weak interactions between oxide surface and N_2. The samples have BET surface areas of 22.6 (MNO-Li), 28.0 (MNO-Na), 7.1 (MNO-K), and 30.5 (CMNO) m^2 g^{-1}. These values are within range of previously reported surface areas for $MnNb_2O_6$[18,25,39] by a variety of synthesis routes. KOH in synthesis reduces the surface area of $MnNb_2O_6$ compared to LiOH and NaOH. H3 hysteresis arises for MNO-Na indicating the plate-like particles are not aggregates, or that the pore network does not fill completely with pore condensate,[40,41] typical of macroporous materials. The average pore widths for these samples, however, are indicative of mesopores, Table S5 (ESI†).

SEM images of the samples from small, Fig. S11 (ESI†), and large batches, Fig. 5, show the size and morphology of the as-made samples. MNO-K shows particles with a walnut shape of a few hundred nanometres, which contrasts with smaller particles when LiOH and NaOH are used. LiOH creates particles with mixed shapes. NaOH gives particles with a carambola shape, formed from thin layers. Substituting 25% of Mn by Ca,

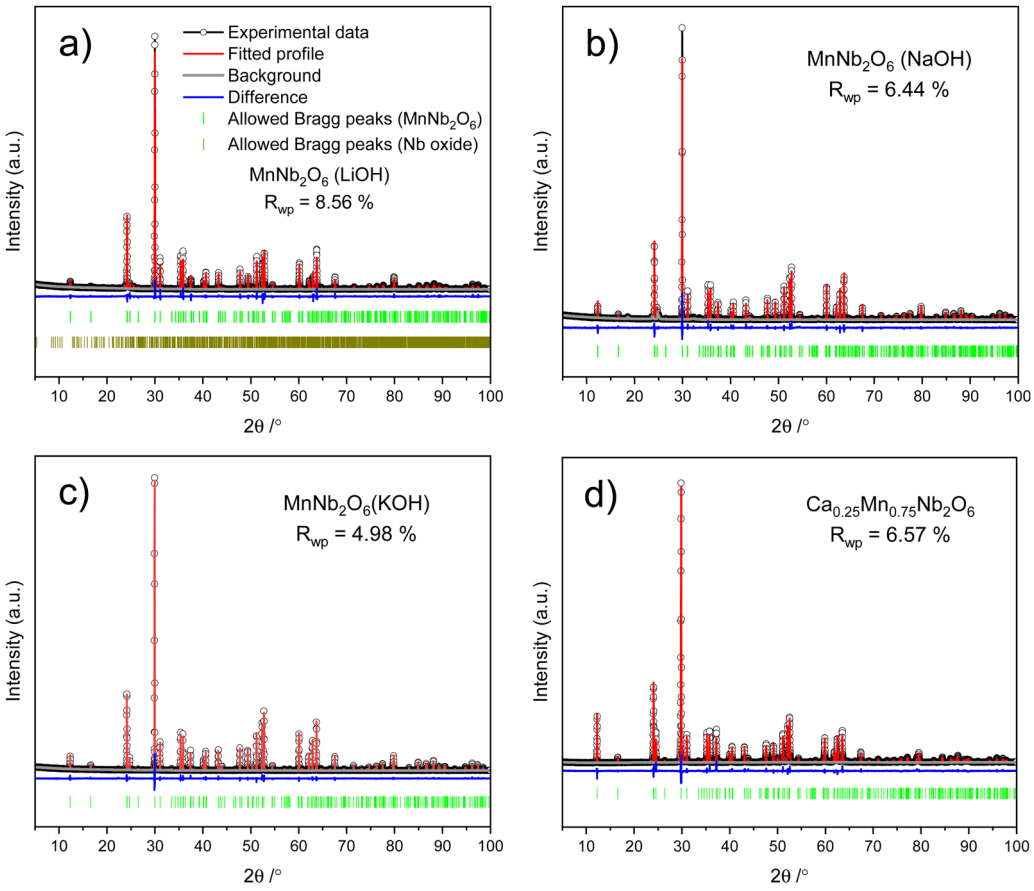

Fig. 3 Rietveld refinement against PXRD (λ = 1.54056 Å) from annealed (a) MNO-Li, (b) MNO-Na, (c) MNO-K, and (d) CMNO using an orthorhombic crystal structure.

the morphology changes with particle size of a few nanometres. Although most of the particles do not have defined shape, some rods are observed in large batches (Fig S12, ESI†). Plate-like particles,[42,43] nanosheets or microneedles,[44] and thin rods[45] morphologies were previously reported for columbite $CaNb_2O_6$ when hydrothermally synthesised. Generally, samples from small batches have similar morphology and particle size to all samples obtained in larger amounts. Previous reports on $MnNb_2O_6$ hydrothermal synthesis using KOH to first form $[Nb_6O_{19}]^{8-}$ followed by reaction with Mn^{2+} in a second step,[22,23,25,26] tended to favour the formation of star-like shaped particles as for some particles synthesised in NaOH seen here. Solvothermally synthesised nanogears[46] and hydrothermally ellipsoid-like structures[24] in a two-step method have been previously described.

Ball milled samples with 5 wt% C65 were imaged using SEM, Fig. S13 (ESI†), showing that the morphology is preserved for all samples after mild energy mixing.

EDS maps were collected to evaluated chemical composition and elemental distribution (Fig. S14, ESI†). Elemental homogeneity of Ca, Mn, Nb and O is confirmed and in Fig. S15 (ESI†), the EDS spectra for MNO-Na, MNO-K and CMNO verify the presence of Na^+, K^+ and Ca^{2+}. $MnNb_2O_6$ has a low percentage of Na^+ and K^+, Fig. S16 (ESI†), indicating the sample might have some alkaline metals at the particles surface even after washing. Since the percentage of Na and K ions are below 0.5%, the structural incorporation of these cations is unlikely.

SEM images of sintered samples for 4 hours, Fig. S17 (ESI†), shows particle growth and no preferred morphology.

XRF was also used for elemental analysis. Table S6 (ESI†) provides the detected metal weight percentages in the samples. The proposed compositions in Table 3 suggest that the percentages of Na^+ and K^+ are low, in agreement with the EDS spectra. Most of the samples are close to the expected molar ratio of Mn : Nb, 1 : 2, besides MNO-Na, 0.78 : 2. This could be due to some amorphous niobium oxide present in the sample, which cannot be determined from a Rietveld refinement. Table S7 (ESI†) summarises and compares the elemental composition from refinement, EDS and XRF data.

For the as-synthesised samples, MNO-Li and MNO-Na, two Nb sites are detected in the XPS data (Fig. 6(a) and (b)). The same is observed for MNO-K, Fig. 6c, when thermally treated at 1000 °C. The surface chemical composition, as shown in the bar graph in Fig. 6d, was calculated and indicates some Na (1.5%) and K (4.8%) ions are present at the materials' surface with close Mn percentages for all three samples. There is no indication of Li ions in the surface, due to the absence of peaks in the Li 1s region (Fig. S18, ESI†). Mn has

Table 2 Structural parameters obtained from Rietveld refinement against PXRD data from sintered MNO-Li, MNO-Na, MNO-K and CMNO. Nb_2O_5 as an extra phase in the MNO-Li is shown separately

Atom	x	y	z	Occupancy	Site	U_{iso}/Å^2
$MnNb_2O_6$ (LiOH) (sintered) R_{wp} = 8.56%, GOF = 3.07, a = 14.4053(1) Å, b = 5.76508(4) Å, c = 5.08094(3) Å, vol = 421.959(3) Å^3, ρ = 4.8017g cm^{-3}. Phase fraction: 0.99087						
Mn	0.0	0.3227(5)	0.25	1.0	4c	0.017(1)
Nb	0.3372(1)	0.3191(2)	0.2443(6)	0.829(4)	8d	*
O	0.0992(5)	0.107(2)	0.063(2)	1.0	8d	0.100(6)
O′	0.4150(4)	0.119(1)	0.097(1)	1.0	8d	0.028(4)
O″	0.7600(6)	0.120(1)	0.087(2)	1.0	8d	0.033(4)
* Nb U_{aniso}	U_{11} 0.0253(8), U_{22} 0.0087(7), U_{33} −0.0068(7), U_{12} −0.001(3), U_{13} 0.002(3), U_{23} 0.001(3)					
$MnNb_2O_6$ (NaOH) (sintered) R_{wp} = 6.64%, GOF = 2.41, a = 14.44382(5) Å, b = 5.76847(2) Å, c = 5.08674(2) Å, vol = 423.820(2) Å^3, ρ = 5.2775 g cm^{-3}						
Mn	0.0	0.3169(4)	0.25	1.0	4c	0.0098(8)
Nb	0.33760(7)	0.3185(1)	0.2412(4)	1.0	8d	0.0094(3)
O	0.0975(3)	0.101(1)	0.063(1)	1.0	8d	0.038(3)
O′	0.4182(3)	0.1118(9)	0.092(1)	1.0	8d	0.00698
O″	0.7598(5)	0.127(1)	0.091(1)	1.0	8d	0.034(3)
$MnNb_2O_6$ (KOH) (sintered) R_{wp} = 4.98%, GOF = 1.88, a = 14.43900(3) Å, b = 5.76737(1) Å, c = 5.08547(1) Å, vol = 423.493(1) Å^3, ρ = 5.2816 g cm^{-3}						
Mn	0.0	0.3200(3)	0.25	1.0	4c	0.0161(5)
Nb	0.33768(5)	0.31915(9)	0.2407(2)	1.0	8d	0.0138(2)
O	0.0986(3)	0.0997(8)	0.056(1)	1.0	8d	0.033(2)
O′	0.4161(2)	0.1165(7)	0.1000(8)	1.0	8d	0.012(2)
O″	0.7595(3)	0.1235(8)	0.0913(9)	1.0	8d	0.026(2)
$Ca_{0.25}Mn_{0.75}Nb_2O_6$ (sintered) R_{wp} = 6.57%, GOF = 2.15, a = 14.51848(9) Å, b = 5.77448(4) Å, c = 5.10064(4) Å, vol = 427.621(3) Å^3, ρ = 5.1802 g cm^{-3}						
Mn	0.0	0.3169(4)	0.25	0.784(1)	4c	0.0116(7)
Ca	0.0	0.3169(4)	0.25	0.216(1)	4c	0.0116(7)
Nb	0.33757(6)	0.3184(1)	0.2360(3)	1.0	8d	0.0130(3)
O	0.1079(3)	0.108(1)	0.056(1)	1.0	8d	0.033(3)
O′	0.4064(2)	0.1168(9)	0.093(1)	1.0	8d	0.00450
O″	0.7631(4)	0.127(1)	0.093(2)	1.0	8d	0.07(3)

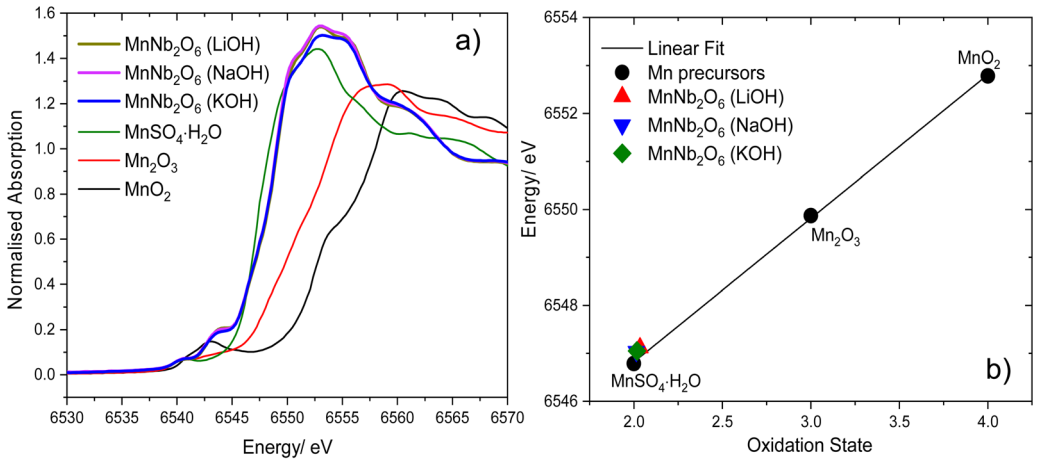

Fig. 4 Mn K-edge XANES (a) $MnNb_2O_6$ in Li, Na and K hydroxides and Mn standards ($MnSO_4{\cdot}H_2O$ (green line), Mn_2O_3 (red line) and MnO_2 (black line)), (b) linear fit from Mn standards including as-made samples.

an oxidation state of 2+ for all samples, which agrees with the binding energy of Mn 2p region,[47] and there is no indication of Mn^{2+} being oxidised when the sample is annealed in air (Fig. S18, ESI†).

The binding energies of Nb in the as-synthesised samples agree with values expected for Nb^{5+}. Further support to this conclusion is confirmed by the difference in binding energy of O 1s and Nb $3d_{5/2}$, which are in the range of 319–324 eV (Tables S8 and S9, ESI†). The values were also compared with some reference samples. Li_3NbO_4[48] and $NaNbO_3$[49] were synthesised as previously reported, whilst NbO_2 and Nb_2O_5 were purchased and used without further treatment. Fig. S19 (ESI†) shows the XPS results for the reference materials. NbO_2 is clearly surface oxidised to Nb^{5+} and, presents low intensity peaks for Nb^{4+} at 208.16 and 205.44 eV. The Nb^{4+} binding energy of ∼206 eV agrees with the literature.[50]

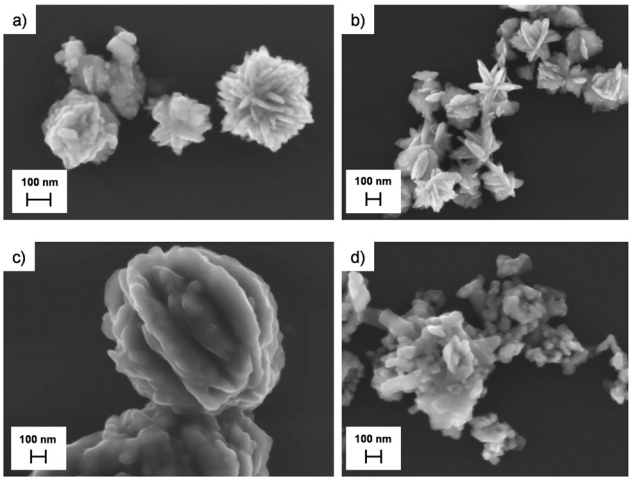

Fig. 5 SEM images of synthesised samples using (a) Li (MNO-Li), (b) Na (MNO-Na) and (c) K (MNO-K) hydroxides and (d) CMNO from large batches. Carbon coated (10 nm) particles, 5 kV, and InLens detector and working distance between 3–6 mm. Scale bar for all images is 100 nm.

Table 3 Measured composition from XRF spectroscopy for all hydrothermally synthesised samples

Sample	Measured composition
MNO-Li	$Mn_{1.15}Nb_{2.00}O_{6.15}$
MNO-Na	$Na_{0.03}Mn_{0.78}Nb_{2.00}O_{5.79}$
MNO-K	$K_{0.04}Mn_{0.90}Nb_{2.00}O_{5.92}$
CMNO	$Ca_{0.13}Mn_{0.69}Nb_{2.00}O_{5.82}$

Because Nb has a non-centrosymmetric O_h environment, the sample surface can be complex and careful consideration is needed to distinguish between Nb^{4+} and Nb^{5+} spin orbit split states, $3d_{5/2}$ and $3d_{3/2}$. Asymmetry could generate "false" Nb^{4+} sites in the surface, which does not reflect the Nb oxide state in the bulk. However, our samples clearly show two distinct Nb^{5+} sites, which may be related to surface and bulk states, or indicate regions of local order and disorder. Previously reported $MnNb_2O_6$ has only two narrow distinguished peaks,[22,23,25,51] which were assigned to Nb^{5+} spin orbit split states and not different sites. The differences in our samples could be associated with the synthesis method. The XPS of both ball-milled MNO-Li and CMNO, in Fig. S20 (ESI†), indicates that the ball milling energy oxidises the surface Mn^{2+} to Mn^{3+}, while Nb 3d spin orbit split states remain in the expected binding energy range for Nb^{5+}. For CMNO one Nb site is more favoured than the other, which is consistent with its ordered structure, compared to Mn niobates. Tables S10 and S11 (ESI†) provide the detailed energy and the energy separation between O 1s and Nb 3d features of ball milled samples.

4. Electrochemical characterisation

Half-coin cells against Li metal were made and the samples were cycled (37 cycles) under different current densities. The average mass loading for all the experiments is given in Table S12 (ESI†). Formation (1st cycle only) was carried out at 10 mA g^{-1}, and in Fig. 7(a) and (b), the 1st and 2nd (at 25 mA g^{-1}) discharge/charge curves are displayed. Initial discharge capacities are 556, 550, 646 mA h g^{-1} for MNO-Li, MNO-Na, and MNO-K, and 474 mA h g^{-1} for CMNO, which has the lowest discharge capacity. The samples lost 44, 43, 54 and 56% of capacity after the first discharge which may be due structural irreversibility, for MNO-Li, MNO-Na, MNO-K and CMNO, respectively. The second cycle appears different from the first cycle, since pseudo-plateaus are observed. The dQ/dV curves in Fig. 7(c–f) show all samples have a plateau $\sim$0.85 V in the first lithiation and a corresponding reversible delithiation at $\sim$1.70 V. Below 0.5 V, there is electrolyte decomposition or a conversion reaction of the active materials. In the second cycle, reversible lithiation ($\sim$1.20 V) and delithiation ($\sim$1.65 V) are observed, but irreversible structural changes occurred around 1–0.5 V for all samples in the first cycle. The materials can accommodate more than 5.6 Li^+ per formula unit in the first lithiation, reducing to below 4 Li^+ in the 2nd lithiation. For example, MNO-K can accommodate more than 8 Li^+. The $MnNb_2O_6$ theoretical capacity is 478 mA h g^{-1} for the insertion of 6 Li^+ to reduce Nb^{5+} to Nb^{3+}. However, the higher capacity achieved for some of the synthesised samples could be an indication of a conversion or mixed insertion/conversion type-electrode. For anode materials, the lithiation/delithiation mechanism is more complicated than in cathodic oxides, due to possible structural changes at low voltages.

Current density studies showed significant capacity reductions at 400 mA g^{-1}, less prominent for CMNO, when compared at 25 mA g^{-1} (Fig. 8). Table 4 summarises the electrochemical performance, and Fig. S21 (ESI†) shows the discharge–charge curves for all samples under different current rates. This drop in specific capacity can be attributed to kinetic limitation in the material,[52] since similar or slightly higher capacities are recovered at 50 mA g^{-1} after 37 cycles (initial average capacities of 174, 155, 124, 200 mA g^{-1}) likely due to activation. The obtained capacities at this current rate are similar for MNO-Li and MNO-Na. MNO-K has lower average capacity compared to all samples, and CMNO has the highest value (Table 4).

The stability and cyclability (200 cycles) of these samples were compared, Fig. 9(a)–(d). MNO-Na has an increase in specific capacity over the first 100 cycles and after 200 cycles the highest specific capacity is observed (Table 5). The same has been observed for molybdenum oxides[30,53] which undergo conversion reactions, but this is the first observation for a Nb-based oxide. The increase in specific capacity is likely due to a conversion reaction, which pulverises the material when cycled, leading to greater electrochemical access to the material and higher surface areas. This is observed from the SEM image after formation (Fig. S22, ESI†). MNO-Li and MNO-K have similar capacities after 50 and 200 cycles. On the other hand, CMNO has the highest capacity after 50 cycles, followed by a reduction upon cycling, see Table 5. Fig. S23 (ESI†) depicts the charge/discharge curves over 200 cycles. Overall, MNO-Li, MNO-Na, MNO-K, and CMNO have average capacity retentions of 35, 64,

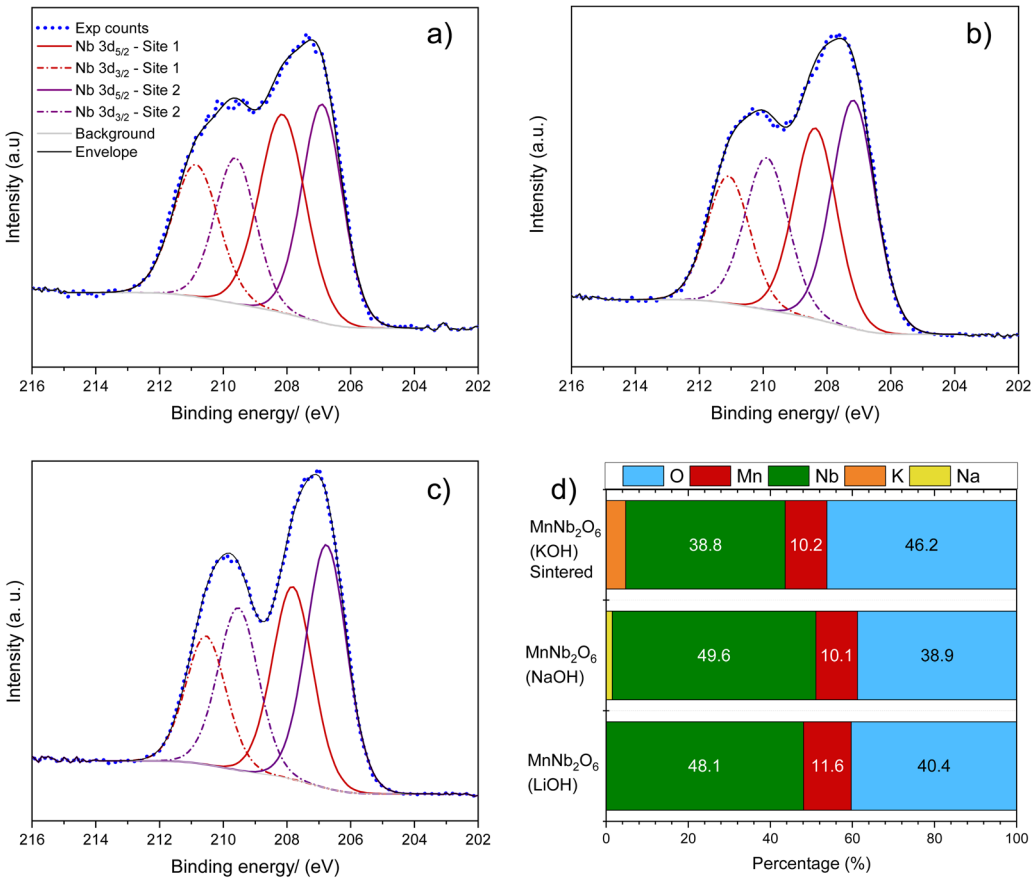

Fig. 6 XPS spectra in the Nb 3d region of hydrothermally synthesised $MnNb_2O_6$ from (a) LiOH, (b) NaOH, (c) annealed KOH and (d) bar graph displaying the surface elemental composition for all three samples.

34, 37%, and the Coulombic efficiency improves to values above 93% after 5 cycles (around 45–57% in the 1st cycle) reaching 100% within 200 cycles. This indicates that the synthesis of MNO in different bases affects the electrochemical properties of the active materials upon Li insertion/extraction. However, replacing Mn^{2+} with Ca^{2+} favours higher initial specific capacities. It confirms that structural expansion increases the Li insertion duration cycling, but the lower capacity in the 1st cycle could be influenced by the insulating properties of Ca.

The samples were cycled in the voltage window of 0.5–2.5 V to minimise irreversible structural changes at low and high potentials. However, all samples presented an impressive capacity reduction, and after 200 cycles MNO-Li, MNO-Na, MNO-K and CMNO achieved capacities corresponding to only 18, 10, 10 and 44% of the capacities in a voltage window of 0.005–3 V. Electrochemical performance, discharge/charge and dQ/dV plots curves are shown in Fig. S24 (ESI†).

The dQ/dV curves along 200 cycles between 0.005–3.0 V revealed similar inversible changes for the first two cycles as observed for the current density studies. MNO-Li and MNO-K have broader peaks with intense and sharper peaks in Fig. S25 (ESI†), but MNO-Na and CMNO have depressed and broader peaks. During delithiation, broader peaks are observed for all samples with their maxima at ~1.7 V in the first cycle, and no oxidation processes happen above 2 V. Whilst cycling, the materials have different electrochemical behaviours, in Fig. S25(b, d, f and h) (ESI†). Oxidation/reduction changes during cycling associated with structural changes upon lithiation/delithiation are observed between 10th and 200th cycles. For MNO-Li, there is decrease in the peak's intensity at 1.09 V shifting to 1.28 V, that is linked to the oxidation process initially at 1.93 V, which shifted to 2.08 V. MNO-Na does not have any redox process at the tenth cycle of high intensities, which suggests an activation process happens, causing the appearance of peaks at 1.47 V (lithiation) and 1.94 V (delithiation). MNO-K does not have any redox chemistry, above 1 V, which explains the lower capacity after cycling. This sample might have a slower activation compared to MNO-Na as the capacity increased from 71 mA h g^{-1} (100th cycle) to 96 mA h g^{-1} (200th cycle). Of all samples, CMNO has the most stable lithiation/delithiation redox chemistry, the peaks became broader and shift to other voltages, which indicates structural changes during lithiation/delithiation and could explain the decrease in capacity upon cycling. Nonetheless, this suggests better structural stability compared to some of the MNO materials.

There are constant changes below 0.5 V for both reduction and oxidation processes when cycling. This could be associated

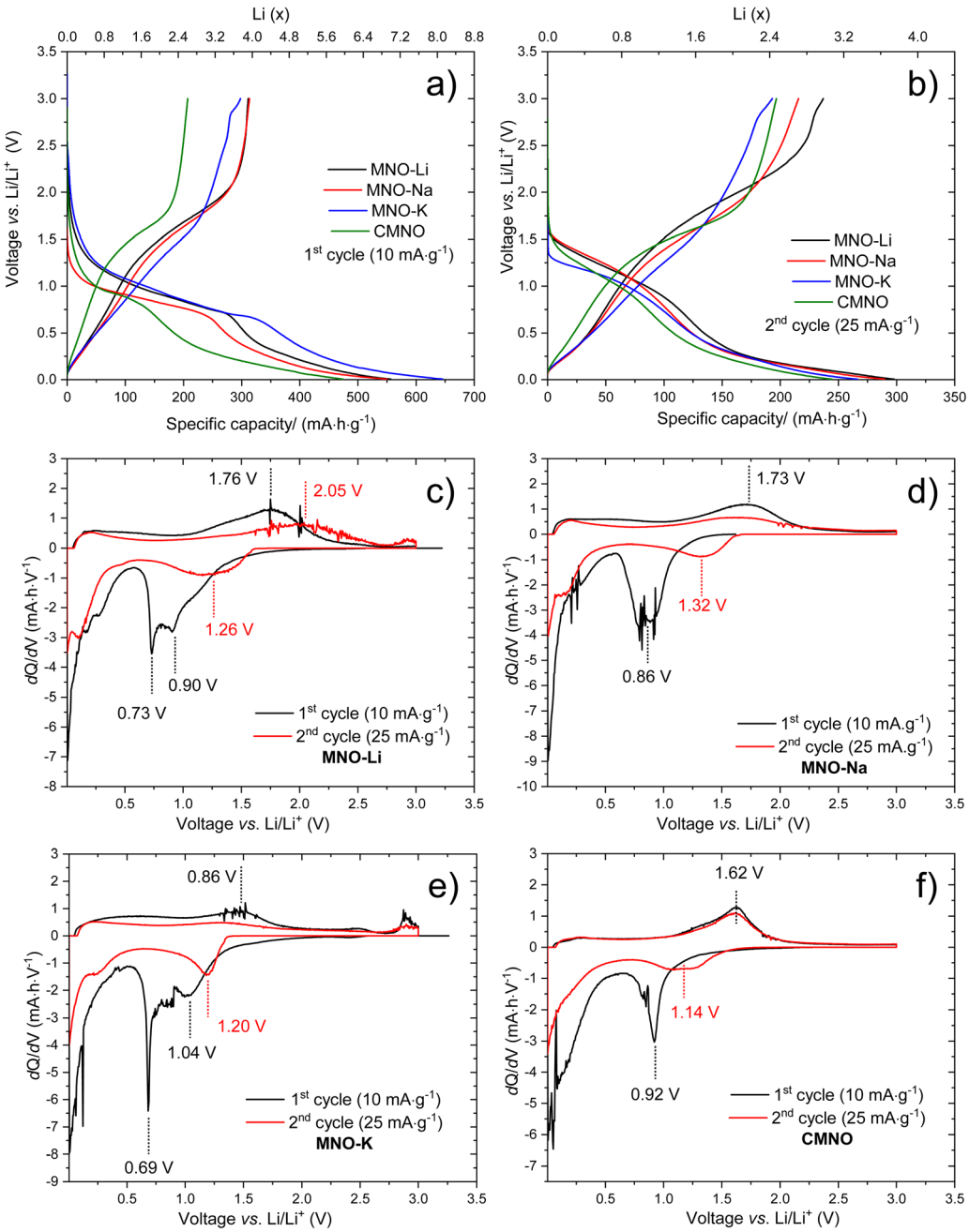

Fig. 7 Electrochemical performance of MNO-Li, MNO-Na, MNO-K, and CMNO half-cells in a voltage window between 0.005–3.0 V for the as-synthesised samples. (a) 1st discharge–charge curves at 10 mA g^{-1}, (b) 2nd discharge–charge curves at 25 mA h g^{-1}, and differential capacity curves (dQ/dV) of (c) MNO-Li, (d) MNO-Na, (e) MNO-K, and (f) CMNO at 1st (25 mA h g^{-1}) and 2nd (25 mA h g^{-1}) cycles between 0.005–3.0 V *vs.* Li/Li^+.

to Li plating[54] and perhaps reduction of Mn^{2+} to Mn^0, which is characteristic of Mn oxides.[6,55–58] The reduction of Nb in anodes from Nb^{5+} to Nb^{3+} is expected to happen in a range of 1.0–2.0 V (in insertion type-electrodes).[8,13] This supports conversion reactions occur below 0.5 V and Nb oxidation/reduction occurs at 0.8 V (lithiation) and 1.78 V (delithiation).

To understand the Li-mechanism, *ex situ* PXRD were collected for samples discharged to 0.005 V and charged to 3.0 V. The PXRD of the as-made electrodes (Fig. S26, ESI†) shows that all samples are crystalline. The relative intensity of MNO-K diffraction peaks is lower compared to the other samples, which is probably correlated to sample thickness. After discharging the samples to 0.005 V, the diffracted peaks' intensity considerably decreased and peak broadening increased. MNO-Na and MNO-K lost the most intense (110) reflection, whilst the others have suffered amorphization (Fig. S27, ESI†). Lee *et al.* have reported *in situ* data from Cu, Mn and Zn niobates,[18] observing the same process during lithiation at 0.01 V. The

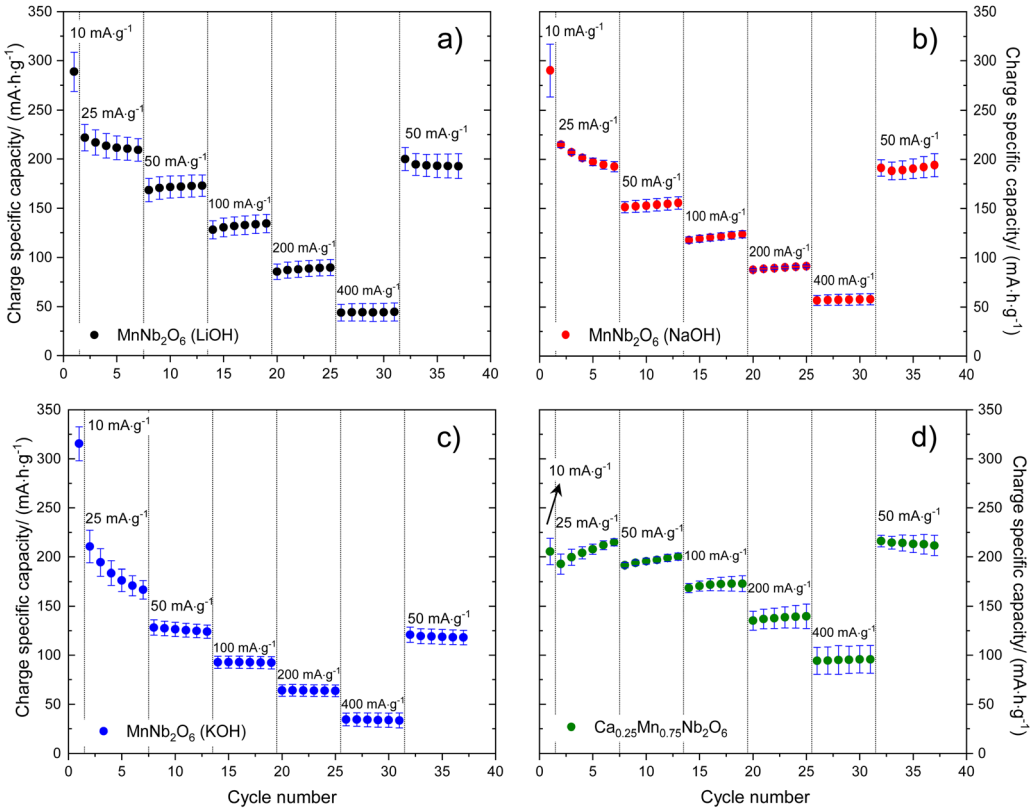

Fig. 8 Cycling under different current densities of half coin cells at 10 mA g^{-1} (1st cycle) and 6 cycles per rate, 25, 50, 100, 200, 400 and 50 mA g^{-1} for (a) MNO-Li, (b) MNO-Na, (c) MNO-K and (d) CMNO in a voltage window between 0.005–3.0 V.

Table 4 Rate performance of MNO-Li, MNO-Na, MNO-K and CMNO

Sample	Rate performance at 400 mA g^{-1}/(mA h g^{-1})	Rate performance at 50 mA g^{-1}/(mA h g^{-1}) after 37 cycles
MNO-Li	44.47 ± 9.20	192.81 ± 12.52
MNO-Na	33.30 ± 7.61	194.09 ± 11.71
MNO-K	58.86 ± 5.77	117.97 ± 7.40
CMNO	95.77 ± 14.07	211.60 ± 10.36

ex situ PXRD supports that the lower electrochemical performance of MNO-K is from irreversible structural changes after the 1st cycle. MNO-Na and CMNO have the best structural stability, maintaining the main diffraction peaks after the first delithiation.

Nyquist plots depict an overall decrease in charge transfer resistance of all electrodes when discharged to 1.0, 0.75 and 0.25 V respectively, Fig. 10. The overall resistivity when charged to 1.0 V (C1.0 V) is lower compared to D1.0V. Bode impedance and phase plots in Fig. S28 (ESI†) reveal a complex insertion/deinsertion mechanism in the MNO and CMNO niobates, which shows changes in Li-ion mechanism in the regions of mid- and low frequencies of 2 kHz and 1 Hz, as observed from the change in phase angle.[59] The Bode phase angle changes from −40° to −20°, which suggests an alternative mechanism besides intercalation (predominant during lithiation at 1.0 V and 0.75 V). This could be associated with a phase change, which occurs during a conversion reaction at these lower voltages. During cycling, the pulverisation of the particles, also creates a larger surface area, which could result in an increase in capacitance from charge storage at the surface of the materials and this would be reflected in a 90° phase angle. This indicates a complex charge storage mechanism, which is not purely due to intercalation or capacitance. Furthermore, SEM images of electrodes after formation showed loss in morphology for MNO-Li and MNO-K, which can be correlated to particle cracking, and pulverisation after the first cycle, Fig. S22 (ESI†), agreeing with loss in crystallinity observed in the in *ex situ* PXRD and the proposed conversion reaction at low voltages. EDS mapping suggests that less Mn is present in all samples compared to the pristine (Fig. S29–S31, ESI†), which is likely to transition metal dissolution in the electrolyte.[60]

Table S13 (ESI†) compares this work with published Mn columbite samples, showing the synthetic route and the electrochemical testing method applied. The materials show electrochemical performance that depends on the synthetic routes, but it is noteworthy most of the previously reported tests used a significantly higher quantity of carbon, which would improve the electronic conductivity of the active material. In our work, we have focussed on using lower amounts of carbon, as 5% or less would be used in a commercial device. Despite this, our

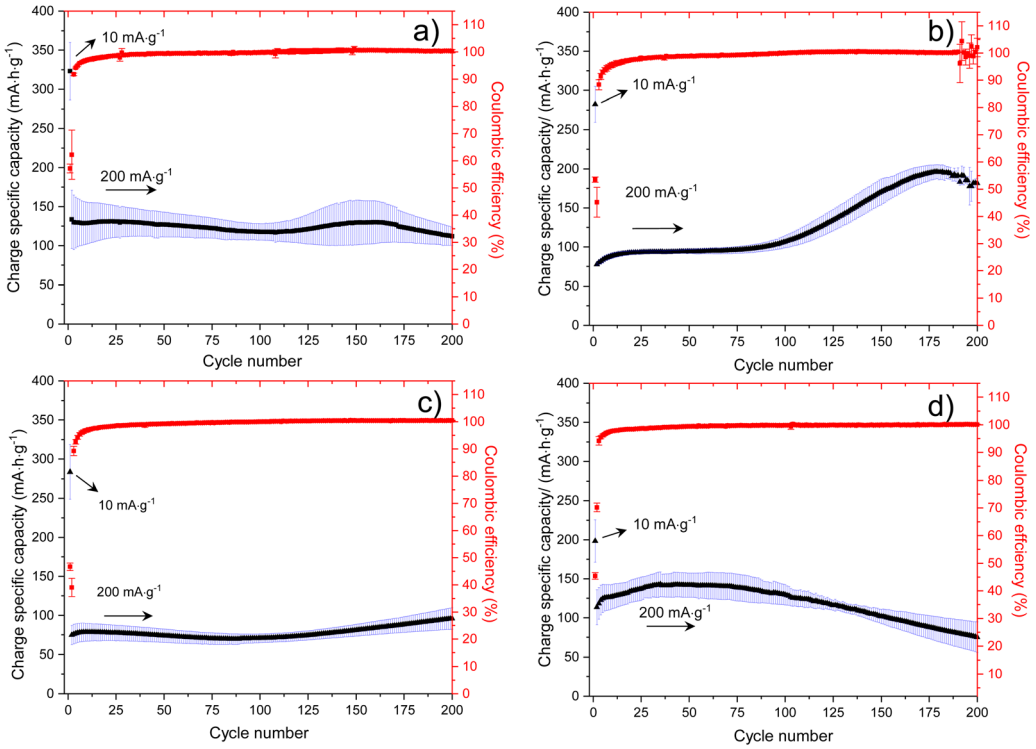

Fig. 9 Electrochemical performance of (a) MNO-Li, (b) MNO-Na, (c) MNO-K, and (d) CMNO half-cells in a voltage window between 0.005–3.0 V. Cyclability tests (200 cycles) and coulombic efficiencies; 1st cycle at 10 mA g^{-1} and 199 cycles at 200 mA h g^{-1}.

Table 5 Cycling performance of MNO-Li, MNO-Na, MNO-K and CMNO

Sample	50th cycle at 200 mA g^{-1}	200th cycle at 200 mA g^{-1}
MNO-Li	127.00 ± 15.88	111.98 ± 11.51
MNO-Na	94.00 ± 2.52	181.53 ± 6.47
MNO-K	73.84 ± 8.54	95.98 ± 13.77
CMNO	141.71 ± 15.46	75.17 ± 19.49

work presents similar or higher capacities in the 1st charge and a better electrochemical performance after 200 cycles for the as-made samples when compared to $MnNb_2O_6$ hydrothermally synthesised in two steps described in the work of Zhang *et al.*[23]

Despite the choice of base having a significant influence on the crystal morphology, which in turn influences electrochemical performance, there is no detectable amount of the alkali cation in the columbite materials prepared in our work. The effect of base on crystal morphology has been reported in the hydrothermal formation of various oxides, including TiO_2,[61] γ-Al_2O_3,[62] ZnO,[63] amorphous IrO_x,[64] and SnO_2.[65] The mechanism of crystal growth has not been systematically investigated, but in the case of titania materials, it has been speculated that intercalation of the alkali-metal cations occurs in an initial step before being expelled leading to the formation of 2D structures and nanorods, with the radius of alkali cation affecting the nanostructure formed.[61] It is conceivable that a similar mechanism is responsible for the formation of the niobates studied in this current work. It is evident that further work is needed to understand the mechanism of hydrothermal crystallisation of oxides, including the role of spectator ions.

Several chemical- and physicochemical techniques must be used to investigate both local and bulk structures to reveal the Li-ion storage mechanism of anodes. In the case of $MnNb_2O_6$, it has been suggested that it has pseudocapacitive properties,[22,23,25,51] which is attributed to materials having a collection of redox sites at various potentials, contributing to the overall electrochemical behaviour. Moreover, a precise Li-mechanism is not being inferred for these materials, but because of the specific capacities from some of the as-made samples are above the theoretical capacity, $MnNb_2O_6$ could collapse to Mn (metal) and Nb^{5+} reducing to Nb^{3+} oxide allowing the formation of Li_2O in an extreme scenario. With this in mind, and the amorphisation process observed for some of materials after the 1st cycle, we suggest that these materials have a conversion-type Li-mechanism in preference of an insertion mechanism supported by electrochemical impedance measurements.

5. Conclusions

A series of columbites $MnNb_2O_6$ and a novel composition $Ca_{0.25}Mn_{0.75}Nb_2O_6$ have been synthesised *via* a hydrothermal method. Heat treatment showed that all samples are pure, and they become ordered upon annealing. Disorder can be understood in the $MnNb_2O_6$ materials by using an ixiolite unit cell,

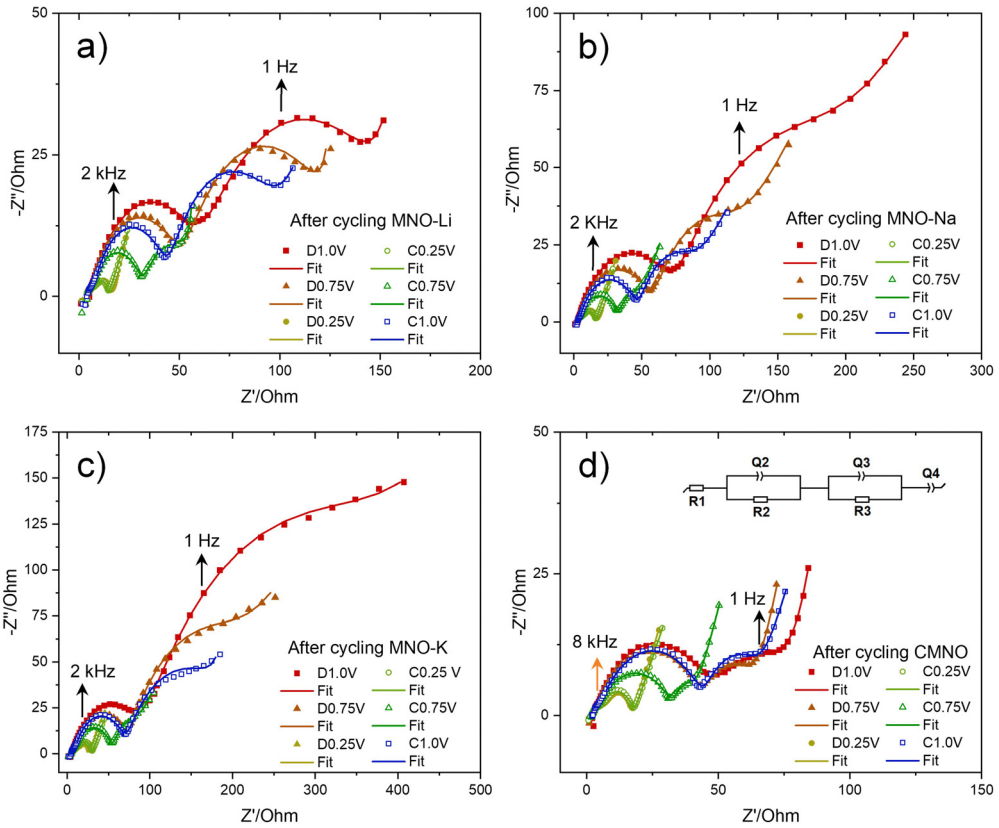

Fig. 10 Nyquist impedance plots of electrodes after 22 cycles (a) MNO-Li, (b) MNO-Na, (c) MNO-K, and (d) CMNO. Fitted circuit depicted in (d), *R* = resistor and *Q* = constant phase element.

but $Ca_{0.25}Mn_{0.75}Nb_2O_6$ has an ordered structure, which may be because of the large ionic radius of Ca. The samples have different electrochemical properties that is correlated to particle size, morphology, and chemical composition. MNO-Na has the best capacity retention after 200 cycles at 200 mA g^{-1} of 64% with capacities around 182 mA h g^{-1}. The Li-storage mechanism for the as-made samples is complex, and likely has an initial intercalation at ~1.6 V *vs.* Li/Li^+ followed by a conversion reaction at lower voltages, as evidenced from the initial capacities above the theoretical capacity of 478 mA h g^{-1}, causing some of the samples to become amorphous or polycrystalline after the 1st lithiation possibly related to Li alloying and particle cracking. This work emphasises the relevance of synthesis in determining the properties of materials for energy storage, opening new avenues to explore ternary Nb-based oxides for their electrochemical properties. Future work is required to better understand the introduction of disorder in the Mn niobates by hydrothermal routes, and further electrochemical testing is important to elucidate structure–property–performance relationships by further optimising electrode formulation to improve their properties.

Conflicts of interest

There are no conflicts to declare.

Acknowledgements

The authors would like to thank CBMM (Companhia Brasileira de Metalurgia e Mineração) for funding this research. We thank the Warwick Manufacturing Group for the facilities at the Energy Innovation Centre. The authors are grateful to David Walker and Steven Huband of the University of Warwick X-ray diffraction facility for aiding in data collection, and Geoff West, Fengzai Tang, and Tom Moore for experimental assistance from the microscopy facility at WMG. We acknowledge James Crosland and Jasmine Clayton for TGA/DSC, and Baiwen Zhao for BET data collection. We thank the University of Warwick's Research Technology Platforms for provision of some of the instrumentation used in this research. M. W. acknowledges financial support from the EPSRC-funded Warwick Analytical Science Centre (EP/V007688/1). Access to B18 was provided by the Energy Materials Block Allocation Group SP14239. We are grateful to Dr Giannantonio Cibin for their help with data acquisition on B18.

References

1 J. Asenbauer, T. Eisenmann, M. Kuenzel, A. Kazzazi, Z. Chen and D. Bresser, The success story of graphite as a lithium-ion anode material - fundamentals, remaining challenges,

and recent developments including silicon (oxide) composites, *Sustainable Energy Fuels*, 2020, **4**, 5387–5416.
2 S. Duehnen, J. Betz, M. Kolek, R. Schmuch, M. Winter and T. Placke, Toward Green Battery Cells: Perspective on Materials and Technologies, *Small Methods*, 2020, **4**, 2000039.
3 Z. Lv, W. Meng, Y. Yang, Y. Zhang, M. Ye and C. C. Li, Nb-based compounds for rapid lithium-ion storage and diffusion, *J. Power Sources*, 2021, **496**, 229840.
4 M. V. Reddy, G. V. S. Rao and B. V. R. Chowdari, Metal Oxides and Oxysalts as Anode Materials for Li Ion Batteries, *Chem. Rev.*, 2013, **113**, 5364–5457.
5 Q. Wang, B. Liu, Y. Shen, J. Wu, Z. Zhao, C. Zhong and W. Hu, Confronting the Challenges in Lithium Anodes for Lithium Metal Batteries, *Adv. Sci.*, 2021, **8**, 2101111.
6 A. Eftekhari, Low voltage anode materials for lithium-ion batteries, *Energy Storage Mater.*, 2017, **7**, 157–180.
7 T. Yuan, Z. P. Tan, C. R. Ma, J. H. Yang, Z. F. Ma and S. Y. Zheng, Challenges of Spinel $Li_4Ti_5O_{12}$ for Lithium-Ion Battery Industrial Applications, *Adv. Energy Mater.*, 2017, **7**, 1601625.
8 H. Ding, Z. Song, H. Zhang and X. Li, Niobium-based oxide anodes toward fast and safe energy storage: a review, *Mater. Today, NANO*, 2020, **11**, 100082.
9 A. Mauger, C. M. Julien, A. Paolella, M. Armand and K. Zaghib, Building Better Batteries in the Solid State: A Review, *Materials*, 2019, **12**, 3892.
10 M. Li, J. Lu, Z. Chen and K. Amine, 30 Years of Lithium-Ion Batteries, *Adv. Mater.*, 2018, **30**, 1800561.
11 Q. Deng, Y. Fu, C. Zhu and Y. Yu, Niobium-Based Oxides Toward Advanced Electrochemical Energy Storage: Recent Advances and Challenges, *Small*, 2019, **15**, 1804884.
12 K. J. Griffith, I. D. Seymour, M. A. Hope, M. M. Butala, L. K. Lamontagne, M. B. Preefer, C. P. Kocer, G. Henkelman, A. J. Morris, M. J. Cliffe, S. E. Dutton and C. P. Grey, Ionic and Electronic Conduction in $TiNb_2O_7$, *J. Am. Chem. Soc.*, 2019, **141**, 16706–16725.
13 L. Hu, L. Luo, L. Tang, C. Lin, R. Li and Y. Chen, $Ti_2Nb_{2x}O_{4+5x}$ anode materials for lithium-ion batteries: a comprehensive review, *J. Mater. Chem. A*, 2018, **6**, 9799–9815.
14 E. J. Kinast, O. Isnard, J. B. M. da Cunha, M. A. Z. de Vasconcellos and C. A. dos Santos, A new approach for the determination of multiple cation locations and ordering, using the example of natural and heat-treated columbites, *J. Appl. Crystallogr.*, 2011, **44**, 738–746.
15 S. Lei, C. Wang, D. Guo, X. Gao, D. Cheng, J. Zhou, B. Chenga and Y. Xiao, Synthesis and magnetic properties of MNb_2O_6 (M = Fe, Co, Ni) nanoparticles, *RSC Adv.*, 2014, **4**, 52740–52748.
16 R. C. Pullar, The Synthesis, Properties, and Applications of Columbite Niobates ($M^{2+}Nb_2O_6$): A Critical Review, *J. Am. Ceram. Soc.*, 2009, **92**, 563–577.
17 P. W. C. Sarvezuk, E. J. Kinast, C. V. Colin, M. A. Gusmao, J. B. M. da Cunha and O. Isnard, Suppression of magnetic ordering in quasi-one-dimensional $Fe_xCo_{1-x}Nb_2O_6$ compounds, *Phys. Rev. B: Condens. Matter Mater. Phys.*, 2011, **83**, 174412.
18 S.-Y. Lee, A. S. Lim, Y. M. Kwon, K. Y. Cho and S. Yoon, Copper, zinc, and manganese niobates ($CuNb_2O_6$, $ZnNb_2O_6$, and $MnNb_2O_6$): structural characteristics, Li^+ storage properties, and working mechanisms, *Inorg. Chem. Front.*, 2020, **7**, 3176–3183.
19 S. C. Tarantino, M. Zema, F. Maglia, M. C. Domeneghetti and M. A. Carpenter, Structural properties of $(Mn_{1-x}Fe_x)Nb_2O_6$ columbites from X-ray diffraction and IR spectroscopy, *Phys. Chem. Miner.*, 2005, **32**, 568–577.
20 S. C. Tarantino, P. Ghigna, C. McCammon, R. Amantea and M. A. Carpenter, Local structural properties of $(Mn,Fe)Nb_2O_6$ from Mossbauer and X-ray absorption spectroscopy, *Acta Crystallogr., Sect. B: Struct. Sci.*, 2005, **61**, 250–257.
21 H. P. Beck, A study on AB_2O_6 compounds, Part II: the branches of the hcp family, *Z. Kristallogr. - Cryst. Mater.*, 2012, **227**, 843–858.
22 T. Wang, T. F. Ma, T. Ge, S. J. Shi, H. M. Ji, W. L. Li and G. Yang, Synthesis of $MnNb_2O_6$ with hierarchical structure as a novel electrode material for high-performance supercapacitors, *J. Alloys Compd.*, 2018, **750**, 428–435.
23 X. Zhang, J. Zhang, S. Kong, K. Zhu, J. Yan, K. Ye, G. Wang, K. Cheng, L. Zhou and D. Cao, A novel calendula-like $MnNb_2O_6$ anchored on graphene sheet as high-performance intercalation pseudocapacitive anode for lithium-ion capacitors, *J. Mater. Chem. A*, 2019, **7**, 2855–2863.
24 S. Lei, D. Guo, C. Wang, D. Cheng, X. Gao, S. Zeng, Y. Xiao and B. Cheng, Preparation and magnetic and microwave absorption properties of $MnNb_2O_6$ ellipsoid-like hierarchical structures, *CrystEngComm*, 2014, **16**, 7949–7955.
25 T. Wang, T. Zhu, J. Wu, Z. Huang, Q. Chen, W. Hu, Y. Huang, S. Shi and W. Yin, The effect of hydrogen induced point defects on lithiation kinetics in manganese niobate anode, *J. Alloys Compd.*, 2021, **877**, 160190.
26 X. Huang, Y. Jing, J. Yang, J. Ju, R. H. Cong, W. L. Gao and T. Yang, Flower-like nanostructure MNb_2O_6 (M = Mn, Zn) with high surface area: Hydrothermal synthesis and enhanced photocatalytic performance, *Mater. Res. Bull.*, 2014, **51**, 271–276.
27 W. Zhang, J. Sheng, J. Zhang, T. He, L. Hu, R. Wang, L. Mai and S. Mu, Hierarchical three-dimensional MnO nanorods/carbon anodes for ultralong-life lithium-ion batteries, *J. Mater. Chem. A*, 2016, **4**, 16936–16945.
28 A. Tandon, S. Rani and Y. Sharma, Designing the Binder-Free Conversion-Based Manganese Oxide Nanofibers as Highly Stable and Rate-Capable Anode for Next-Generation Li-Ion Batteries, *ACS Appl. Energy Mater.*, 2022, **5**, 6855–6868.
29 H. Wang, T. Y. Li, A. M. Hashem, A. E. Abdel-Ghany, R. S. El-Tawil, H. M. Abuzeid, A. Coughlin, K. Chang, S. X. Zhang, H. El-Mounayri, A. Tovar, L. K. Zhu and C. M. Julien, Nanostructured Molybdenum-Oxide Anodes for Lithium-Ion Batteries: An Outstanding Increase in Capacity, *Nanomaterials*, 2022, **12**, 13.
30 D. Wu, R. Shen, R. Yang, W. X. Ji, M. Jiang, W. P. Ding and L. M. Peng, Mixed Molybdenum Oxides with Superior

Performances as an Advanced Anode Material for Lithium-Ion Batteries, *Sci. Rep.*, 2017, **7**, 44697.

31 H. Kim, C.-D. Lee, D. I. Kim, W. Choi, D.-H. Seo and W.-S. Yoon, Bonding dependent lithium storage behavior of molybdenum oxides for next-generation Li-ion batteries, *J. Mater. Chem. A*, 2022, **10**, 7718–7727.

32 B. H. Toby and R. B. Von Dreele, GSAS-II: the genesis of a modern open-source all purpose crystallography software package, *J. Appl. Crystallogr.*, 2013, **46**, 544–549.

33 N. Fairley, V. Fernandez, M. Richard-Plouet, C. Guillot-Deudon, J. Walton, E. Smith, D. Flahaut, M. Greiner, M. Biesinger, S. Tougaard, D. Morgan and J. Baltrusaitis, Systematic and collaborative approach to problem solving using X-ray photoelectron spectroscopy, *Appl. Surf. Sci. Adv.*, 2021, **5**, 100112.

34 A. J. Dent, G. Cibin, S. Ramos, A. D. Smith, S. M. Scott, L. Varandas, M. R. Pearson, N. A. Krumpa, C. P. Jones and P. E. Robbins, B18: A core XAS spectroscopy beamline for Diamond, *J. Phys.: Conf. Ser.*, 2009, **190**, 012039.

35 B. Ravel and M. Newville, ATHENA, ARTEMIS, HEPHAESTUS: data analysis for X-ray absorption spectroscopy using IFEFFIT, *J. Synchrotron Radiat.*, 2005, **12**, 537–541.

36 E. H. Nickel, J. F. Rowland and R. C. McAdam, Ixiolite—A Columbite Substructure, *Am. Mineral.*, 1963, **48**, 961–979.

37 C. Tealdi, M. C. Mozzati, L. Malavasi, T. Ciabattoni, R. Amantea and C. B. Azzoni, Columbite-type $Fe_xMn_{1-x}Nb_2O_6$ solid solution: structural and magnetic characterization, *Phys. Chem. Chem. Phys.*, 2004, **6**, 4056–4061.

38 J. P. Cummings and S. F. Simonsen, The crystal structure of calcium niobate ($CaNb_2O_6$), *Am. Mineral.*, 1970, **55**, 90–97.

39 T. Wang, S. J. Shi, F. J. Kong, G. Yang, B. Qian and F. Yin, The role of stable interface in nano-sized $FeNbO_4$ as anode electrode for lithium-ion batteries, *Electrochim. Acta*, 2016, **203**, 206–212.

40 M. Thommes, K. Kaneko, A. V. Neimark, J. P. Olivier, F. Rodriguez-Reinoso, J. Rouquerol and K. S. W. Sing, Physisorption of gases, with special reference to the evaluation of surface area and pore size distribution (IUPAC Technical Report), *Pure Appl. Chem.*, 2015, **87**, 1051–1069.

41 K. A. Cychosz, R. Guillet-Nicolas, J. Garcia-Martinez and M. Thommes, Recent advances in the textural characterization of hierarchically structured nanoporous materials, *Chem. Soc. Rev.*, 2017, **46**, 389–414.

42 I.-S. Cho, D. W. Kim, C. M. Cho, J.-S. An, H.-S. Roh and K. S. Hong, Synthesis, characterization and photocatalytic properties of $CaNb_2O_6$ with ellipsoid-like plate morphology, *Solid State Sci.*, 2010, **12**, 982–988.

43 I.-S. Cho, D. W. Kim, T. H. Noh, S. Lee, D. K. Yim and K. S. Hong, Preparation of N-Doped $CaNb_2O_6$ Nanoplates with Ellipsoid-Like Morphology and Their Photocatalytic Activities Under Visible-Light Irradiation, *J. Nanosci. Nanotechnol.*, 2010, **10**, 1196–1202.

44 Y. Zhang, C. Liu, G. Pang, S. Jiao, S. Zhu, D. Wang, D. Liang and S. Feng, Hydrothermal Synthesis of a $CaNb_2O_6$ Hierarchical Micro/Nanostructure and Its Enhanced Photocatalytic Activity, *Eur. J. Inorg. Chem.*, 2010, 1275–1282.

45 M. Hirano, T. Iwata, K. Komaki, H. Iwata and K. Tanaka, Hydrothermal synthesis of luminescent niobate thin rods, *J. Ceram. Soc. Jpn.*, 2020, **128**, 875–882.

46 W. B. Hu, Z. C. Cui and Y. Z. Mi, 3-D $MnNb_2O_6$ nanogears from 1-D Nb_2O_5 nanorods, *Mater. Chem. Phys.*, 2012, **133**, 599–604.

47 M. C. Biesinger, B. P. Payne, A. P. Grosvenor, L. W. M. Lau, A. R. Gerson and R. S. Smart, Resolving surface chemical states in XPS analysis of first row transition metals, oxides and hydroxides: Cr, Mn, Fe, Co and Ni, *Appl. Surf. Sci.*, 2011, **257**, 2717–2730.

48 N. Yabuuchi, M. Takeuchi, M. Nakayama, H. Shiiba, M. Ogawa, K. Nakayama, T. Ohta, D. Endo, T. Ozaki, T. Inamasu, K. Sato and S. Komaba, High-capacity electrode materials for rechargeable lithium batteries: Li_3NbO_4-based system with cation-disordered rocksalt structure, *Proc. Natl. Acad. Sci. U. S. A.*, 2015, **112**, 7650–7655.

49 D. R. Modeshia, R. J. Darton, S. E. Ashbrook and R. I. Walton, Control of polymorphism in $NaNbO_3$ by hydrothermal synthesis, *Chem. Commun.*, 2009, 68–70.

50 G. J. P. Fajardo, S. A. Howard, E. Evlyukhin, M. J. Wahila, W. R. Mondal, M. Zuba, J. E. Boschker, H. Paik, D. G. Schlom, J. T. Sadowski, S. A. Tenney, B. Reinhart, W.-C. Lee and L. F. J. Piper, Structural Phase Transitions of NbO_2: Bulk versus Surface, *Chem. Mater.*, 2021, **33**, 1416–1425.

51 Y. Lian, Y. Zheng, D. Wang, Y. Bai, H. Yan, Z. Wang, J. Zhao and H. Zhang, Ultrafast and stable ion/electron transport of $MnNb_2O_6$ in LIC/SC via interface protection and lattice defects, *J. Colloid Interface Sci.*, 2022, **606**, 77–86.

52 Y. Kim, Q. Jacquet, K. J. Griffith, J. Lee, S. Dey, B. L. D. Rinkel and C. P. Grey, High Rate Lithium Ion Battery with Niobium Tungsten Oxide Anode, *J. Electrochem. Soc.*, 2021, **168**, 010525.

53 U. K. Sen and S. Mitra, Synthesis of Molybdenum Oxides and their Electrochemical Properties against Li, *Energy Procedia*, 2014, **54**, 740–747.

54 Q. Q. Liu, C. Y. Du, B. Shen, P. J. Zuo, X. Q. Cheng, Y. L. Ma, G. P. Yin and Y. Z. Gao, Understanding undesirable anode lithium plating issues in lithium-ion batteries, *RSC Adv.*, 2016, **6**, 88683–88700.

55 X. M. Tang, G. Sui, Q. Cai, W. H. Zhong and X. P. Yang, Novel MnO/carbon composite anode material with multimodal pore structure for high performance lithium-ion batteries, *J. Mater. Chem. A*, 2016, **4**, 2082–2088.

56 X. P. Fang, X. Lu, X. W. Guo, Y. Mao, Y. S. Hu, J. Z. Wang, Z. X. Wang, F. Wu, H. K. Liu and L. Q. Chen, Electrode reactions of manganese oxides for secondary lithium batteries, *Electrochem. Commun.*, 2010, **12**, 1520–1523.

57 M. A. Lowe, J. Gao and H. D. Abruna, In operando X-ray studies of the conversion reaction in Mn_3O_4 lithium battery anodes, *J. Mater. Chem. A*, 2013, **1**, 2094–2103.

58 I. A. Ayhan, Q. Li, P. Meduri, H. Oh, G. R. Bhimanapati, G. Yang, J. A. Robinson and Q. Wang, Effect of Mn_3O_4 nanoparticle composition and distribution on graphene as a potential hybrid anode material for lithium-ion batteries, *RSC Adv.*, 2016, **6**, 33022–33030.

59 N. Meddings, M. Heinrich, F. Overney, J. S. Lee, V. Ruiz, E. Napolitano, S. Seitz, G. Hinds, R. Raccichini, M. Gabers and J. Park, Application of electrochemical impedance spectroscopy to commercial Li-ion cells: A review, *J. Power Sources*, 2020, **480**, 228742.

60 J. P. Allen and C. P. Grey, Determining the oxidation states of dissolved transition metals in battery electrolytes from solution NMR spectra, *Chem. Commun.*, 2023, **59**, 1677–1680.

61 L. M. Sikhwivhilu, S. S. Ray and N. J. Coville, Influence of bases on hydrothermal synthesis of titanate nanostructures, *Appl. Phys. A: Mater. Sci. Process.*, 2009, **94**, 963–973.

62 M. Abdollahifar, Synthesis and characterisation of γ-Al_2O_3 with porous structure and nanorod morphology, *J. Chem. Res.*, 2014, **38**, 154–158.

63 Y. Im, S. Kang, B. S. Kwak, K. S. Park, T. W. Cho, J. S. Lee and M. Kang, Electrochemical performance of three shaped ZnO nanoparticles prepared in LiOH, NaOH and KOH alkaline solutions as anodic materials for Ni/Zn redox batteries, *Korean J. Chem. Eng.*, 2016, **33**, 1447–1455.

64 J. R. Esquius, D. J. Morgan, I. Spanos, D. G. Hewes, S. J. Freakley and G. J. Hutchings, Effect of Base on the Facile Hydrothermal Preparation of Highly Active IrO_x Oxygen Evolution Catalysts, *ACS Appl. Energy Mater.*, 2020, **3**, 800–809.

65 K. Sato, Y. Yokoyama, J. C. Valmalette, K. Kuruma, H. Abe and T. Takarada, Hydrothermal Growth of Tailored SnO_2 Nanocrystals, *Cryst. Growth Des.*, 2013, **13**, 1685–1693.